






# Benchmarking Machine Learning Models for Multi-Class State Recognition in Double Quantum Dot Data

Valeria Díaz Moreno<sup>1,\*</sup> , Ryan P Khalili<sup>1,\*</sup> , Daniel Schug<sup>2</sup> , Patrick J. Walsh<sup>1,3</sup> , Justyna P. Zwolak<sup>4,5,6,†</sup> 

<sup>1</sup>Department of Physics, University of Wisconsin-Madison, Madison, Wisconsin 53706, USA

<sup>2</sup>Department of Computer Science, University of Maryland, College Park, MD 20742, USA

<sup>3</sup>Department of Applied Physics, Stanford University, Stanford, California 94305, USA

<sup>4</sup>National Institute of Standards and Technology, Gaithersburg, MD 20899, USA

<sup>5</sup>Joint Center for Quantum Information and Computer Science, University of Maryland, College Park, Maryland 20742, USA

<sup>6</sup>Department of Physics, University of Maryland, College Park, Maryland 20742, USA

\*These authors contributed equally to this work.

†Author to whom any correspondence should be addressed.

**E-mail:** jpzwolak@nist.gov

**Keywords:** quantum dots; machine learning; automated tuning; benchmarking

## Abstract

Semiconductor quantum dots (QDs) are a leading platform for scalable quantum processors. However, scaling to large arrays requires reliable, automated tuning strategies for devices' bootstrapping, calibration, and operation, with many tuning aspects depending on accurately identifying QD device states from charge-stability diagrams (CSDs). In this work, we present a comprehensive benchmarking study of four modern machine learning (ML) architectures for multi-class state recognition in double-QD CSDs. We evaluate their performance across different data budgets and normalization schemes using both synthetic and experimental data. We find that the more resource-intensive models—U-Nets and visual transformers (ViTs)—achieve the highest MSE score (defined as  $1 - \text{MSE}$ ) on synthetic data (over 0.98) but fail to generalize to experimental data. MDNs are the most computationally efficient and exhibit highly stable training, but with substantially lower peak performance. CNNs offer the most favorable trade-off on experimental CSDs, achieving strong accuracy with two orders of magnitude fewer parameters than the U-Nets and ViTs. Normalization plays a nontrivial role: min-max scaling generally yields higher MSE scores but less stable convergence, whereas z-score normalization produces more predictable training dynamics but at reduced accuracy for most models. Overall, our study shows that CNNs with min-max normalization are a practical approach for QD CSDs.

## 1 Introduction

Semiconductor quantum dot (QD) spin qubits are one of several promising platforms for quantum computing. In QDs, the quantum information is encoded in the spin state of a single or few isolated charges [1, 2]. With appropriate gating and materials engineering, the spin states  $\{|\uparrow\rangle, |\downarrow\rangle\}$  form a natural computational basis, while electrostatic gates enable initialization, manipulation, and readout within an integrated, CMOS-compatible platform [3]. In  $\text{Si}_x\text{Ge}_{1-x}$  heterostructures, a strained Si quantum well forms the conduction channel, and metal gates locally modulate the electrostatic potential to define one or more QDs and proximal charge sensors in a two-dimensional electron gas (2DEG) [4]. This architecture supports high-fidelity spin control and remains a leading route toward scalable, densely integrated quantum processors [1].

To reach target charge states and tunnel coupling between QDs, tens of gate voltages need to be adjusted to bring the QD device into its operating regime. The tuning process involves repeated current- or conductance-based measurements, in which one or two gate voltages are swept while the QD device response is monitored, followed by careful adjustment of selected gate voltages [5]. Even tuning a double quantum dot (DQD) is a nontrivial task. Forming two QDs with a desired number of charges on each dot and the required lead and interdot couplings requires simultaneous adjustment of at least three metallic gates per QD, with significant cross-capacitance between them. As the number of dots grows, scripted tuning approaches become increasingly impractical. Such tuning does not scale: larger QD arrays multiply gate cross-talk, drift, device-to-device

variability, and measurement overhead. Consequently, there is a strong interest in autonomous tuning using machine learning (ML) [6].

*Charge stability diagrams* (CSDs) [5]—2D measurements in the space of two plunger gates, i.e., gates that control the QD chemical potential—are especially prevalent in the later tuning stages, including state tuning [7], setting desired charge configurations [8], establishing controllability [9–11], and detecting unintended QD formation [12]. CSDs are typically acquired with a proximal charge sensor, i.e., an auxiliary QD biased for high transconductance that yields sharp contrast when the DQD occupancy changes. CSDs compactly reveal information about QD formation, cross-capacitances, interdot coupling, and charge transition topology, and thus serve as the canonical diagnostic for state identification and device control.

However, the availability of labeled, high-quality data necessary for training and testing ML models remains a persistent bottleneck in the realm of QD autotuning. While CSDs can be collected rapidly, manual labeling by experts is time-consuming, can be ambiguous, and is prone to bias and error. As a result, most supervised ML models for CSD implemented in QD tuning algorithms rely on simulated data paired with realistic instrument and device noise models [6]. This has motivated the 2017 release of a first large dataset containing idealized and increasingly noisy simulated CSDs [13], followed by publication of several open-source QD device simulators [14–17]. At the same time, questions arose about the validity of ML models trained exclusively on simulated data, motivating systematic benchmarking of ML models trained using simulated and experimental data.

In response, Darulová *et al.* compared several families of ML models, ranging from simple logistic regression to convolutional neural networks (CNNs), trained on synthetic, experimental, and mixed CSD datasets for a simplified, binary state recognition (single- vs. double-QD state). They found that CNNs performed best, with mixed synthetic and experimental training reaching 89.5 % accuracy, about 10 % higher than training only with experimental data. Simpler models typically achieved  $\sim 45$  % to 75 % accuracy. They also highlighted the sensitivity of CNNs to the quality of synthetic noise models, suggesting that synthetic noise that does not properly mimic experimental noise can impair proper training. Since then, the field has shifted toward implementing more complex models, including deeper CNNs, U-Net architectures, and transformer backbones. However, the practical necessity of such complexity remains unclear relative to simpler baselines, especially under constrained data budgets and across variable acquisition settings.

Building on these efforts, we benchmark modern ML approaches for *multi-class* state recognition in CSDs of double QD devices, using more varied synthetic CSDs and an expanded evaluation protocol. Our goals are to quantify performance across model families as a function of dataset size and to provide a transparent, reproducible baseline and dataset splits to facilitate fair comparison in future autotuning protocols. We benchmark representative classical and deep models using consistent training and evaluation protocols, reporting accuracy, calibration, and data-efficiency curves for all tested cases. Specifically, we

- benchmark four model families on *multi-class* DQD state recognition with fractional labels;
- quantify accuracy vs compute (GPU/CPU time, memory, parameters) across data budgets and normalizations; and
- release a unified, reproducible benchmarking framework.

The paper is organized as follows: section 2 provides a brief overview of the scientific context of the problem. Section 2.1 describes the problem of control and tuning QD devices. Data used for benchmarking is discussed in section 2.2 and the ML methods considered in this work are described in sections 2.3 through 2.6. The performance comparison is presented in section 3. We conclude with a discussion of the future direction in section 4.

## 2 Background and methods

In this section, we introduce the scientific context of our problem and the data utilized in our experiments. A brief overview of all ML models used in our study, together with example applications in sciences, with convolutional neural networks (CNNs) discussed in section 2.3, U-Net architectures in section 2.4, vision transformers (ViTs) in section 2.5, and mixture density networks (MDNs) in section 2.6. The model training configuration is presented in section 2.7. We conclude with a short description of a ML *mini-suite* for QD CSDs, which we make publicly available on GitHub [18] as part of this work.

### 2.1 Physics problem

Semiconductor QDs are formed by electrostatic confinement created by lithographic gates and the underlying material stack: vertical/axial confinement arises from quantum wells, band offsets, or

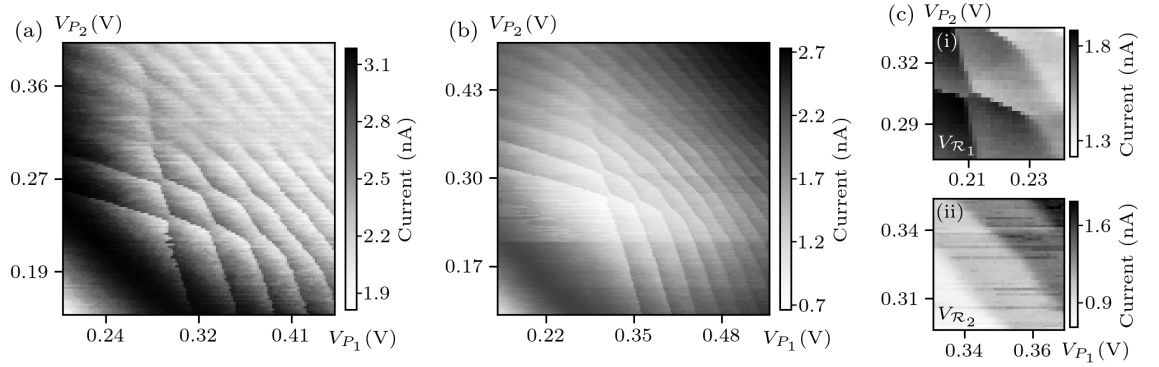


**Figure 1.** (a-b) Two examples of large and (c) small experimentally acquired charge stability diagrams included in the *QFlow 2.0: Quantum dot data for machine learning* dataset [13]. The manually assigned labels for the small charge stability diagrams are  $\mathbf{p}(V_{\mathcal{R}_1}) = (0, 0, 0.1, 0, 0.9)$  for (c-i) and  $\mathbf{p}(V_{\mathcal{R}_2}) = (0, 0, 1, 0, 0)$  for (c-ii).

accumulation/inversion layers (Si/SiGe, Ge/SiGe, GaAs/AlGaAs, MOS), while lateral confinement is set by patterned gates or nanowire geometries that define one or more dots and their couplings [1, 2, 19]. For a typical one-dimensional array of QDs, pairs of *barrier* gates define tunnel barriers to the reservoirs and to neighboring QDs, while *plunger* gates tune the QD chemical potential. In the smallest multi-QD systems, the double-QD (DQD) devices, there are at least five gates necessary for full control: two plunger gates set the left/right dot chemical potentials, and three barriers (source, interdot, drain) tune the tunnel couplings to reservoirs and between dots [5].

Depending on the applied plunger voltages, the DQD device can realize five common operating regimes that serve as labels in most works on QD device autotuning: no-dot (ND), left ( $SD_L$ ), right ( $SD_R$ ), and merged central- ( $SD_C$ ) single-QD, and double-dot (DD). A central diagnostic for identifying these regimes is the CSD obtained by sweeping the two plunger gates while monitoring a proximal charge sensor [20]. Changes in QD occupancy alter the sensor conductance, resulting in characteristic transition lines whose topology encodes QD formation, cross-capacitances, and interdot coupling. Two examples of experimentally acquired CSD for DQD systems in the space of plunger voltages ( $V_{P_1}, V_{P_2}$ ) are depicted in figure 1(a-b). The lower left corner of these plots corresponds to the ND state. Increasing voltage on the plunger  $P_1$  ( $P_2$ ) increases the occupation of the right (left) QD, starting at zero and increasing by one charge every time a line is crossed. Increasing both plunger voltages simultaneously increases the occupation on both QD. At large plunger voltages, the two separate QD merge into a single central QD.

Manually determining the operating voltages is challenging because cross-capacitance, tunnel-coupling trade-offs, and the gate topology that ties multiple QDs to the same gate make the voltages highly co-dependent. Moreover, operating points vary across devices and between cooldowns owing to nanofabrication variability and trapped charge in the gate-oxide stack, which shift local accumulation thresholds and drift over time. These factors make repeated CSD measurements and interpretation a dominant bottleneck for scaling. To address this, modern autotuning algorithms for QD devices implement ML-enabled automated interpretation of CSD, utilizing more cost-effective, smaller CSDs, as shown in figure 1. To date, several studies have shown that ML models trained exclusively on *synthetic* CSDs augmented by realistic instrument and device noise generalize extraordinarily well to experimental data [6].

## 2.2 Dataset description

This work utilizes the *QFlow 2.0: Quantum dot data for machine learning* (hereafter referred to as QFlow 2.0) dataset [13]—a curated collection of synthetic and experimental CSD—created to enable ML-driven calibration and control of QD devices [21]. The simulated CSDs included in QFlow 2.0 were generated using a modified Thomas–Fermi approximation of a quasi-1D nanowire controlled by five depletion gates whose voltages determine QD formation, charge occupancy, and conductance. QFlow 2.0 dataset consists of  $1.6 \times 10^4$  large synthetic CSDs representing 1,599 simulated devices, each with 10 random noise realizations that reflect experimentally observed variability. The simulated CSDs are stored as  $250 \times 250$  NumPy arrays, see figure 2(a), together with the corresponding state label array identifying the state of the device at each pixel, see figure 2(b), the plunger-gate axes ( $V_{P_1}, V_{P_2}$ ), and metadata describing device parameters and noise settings.

To create the training and testing dataset used in this work, 10 small, ( $30 \times 30$ ) pixel patches

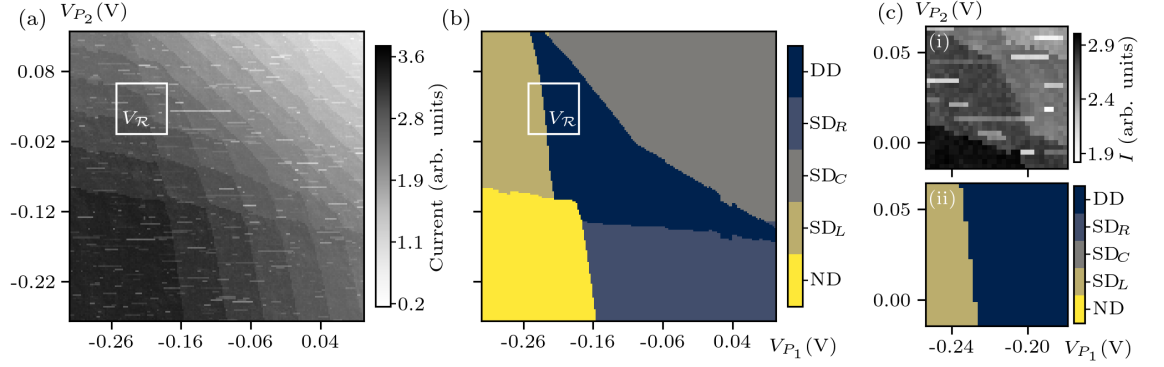


**Figure 2.** (a) A sample synthetic charge stability diagram and (b) the corresponding state map from the *QFlow 2.0: Quantum dot data for machine learning* dataset [13]. The state map labels correspond to the five possible states for a double-QD device: no-dot (ND), left ( $SD_L$ ), central ( $SD_C$ ), and right ( $SD_R$ ) single-dot, and double-dot (DD). (c-i) An example patch  $V_R$  sampled from the CSD, highlighted in panel (a) with a white rectangle. (c-ii) A State label patch corresponding to the example patch shown in panel (c-i), highlighted in panel (b) with a white rectangle. The assigned state label vector for this patch is  $\mathbf{p}(V_R) = (0, 0.3, 0, 0, 0.7)$ .

were randomly sampled from each synthetic CSD, yielding 159,900 samples. The patch size was chosen to avoid upscaling experimental CSDs, which range in size from  $(30 \times 30)$  pixel to  $(60 \times 60)$  pixel with 1 mV- to 2 mV-per-pixel resolution, as it could introduce unphysical features. Each sample includes the CSD subarray together with the corresponding label subarray, the local voltage coordinates, the patch center within the parent CSD, the parent CSD identifier, and a noise identifier. An example CSD patch and the corresponding label subarray are shown in figure 2(c-i) and figure 2(c-ii), respectively.

It is important to stress that in the context of tuning QD arrays, it is possible, and often desirable, to capture multiple QD states within a single small CSD, as shown in figure 2(c-i). The multi-state nature of the small CSDs is captured by fractional ground-truth labels derived from the label subarrays, which are formally encoded as five-dimensional vectors:

$$\mathbf{p}(V_R) = (p_{ND}, p_{SD_L}, p_{SD_C}, p_{SD_R}, p_{DD}) \quad (1)$$

where  $p_X$ , with  $X \in \{ND, SD_L, SD_C, SD_R, DD\}$ , indicates the fraction of pixels within a CSD belonging to each of the five states. The fractional, multi-valued labels are intended to indicate an intermediate, transitional state of the QD device rather than confusion [22].

To enable performance comparison, all ML models are trained under controlled data and normalization settings. First, we set aside 9,900 random samples for final testing, keeping the remaining 150,000 samples for training and validation. We then construct four data-budget conditions: 25 % (37,500,  $\mathcal{D}_1$ ), 50 % (75,000,  $\mathcal{D}_2$ ), 75 % (112,500,  $\mathcal{D}_3$ ), and 100 % (150,000,  $\mathcal{D}_4$ ) samples. For each data budget, we train under two normalization schemes: (i) *Gaussian standardization* (z-score; mean=0, standard deviation=1) and (ii) *min-max* scaling (min=0, max=1). This amounts to 8 distinct training runs for each model.

### 2.3 Convolutional neural networks

Convolutional neural networks (CNNs) use learned local filters and pooling to capture spatial hierarchies in images and grids, making them natural for scientific data with spatial structure [23]. In the physical sciences, CNNs have been adopted for tasks such as phase identification and diffraction-pattern analysis in materials [24, 25] to galaxy morphology classification in astronomy [26] and atomic-defect identification in scanning probe microscopy [27]. For quantum-dot (QD) control, CNNs have been used for charge-state recognition [21, 28] and data-quality assessment on charge-stability diagrams, enabling robust autotuning pipelines [29]. CNNs were applied to in-line SEM micrographs to assess device usability by detecting fabrication defects such as particle contamination and under-/over-exposure [30].

The CNN architecture employed in this work is largely based on previous demonstrations of CNN-based autotuning for QD devices [29]. The network comprises four convolutional blocks with ReLU activations, interleaved with dropout for regularization and followed by adaptive average pooling. The final fully connected layer produces a five-way probability vector.

#### 2.4 U-Net classifiers

U-Net augments a convolutional backbone with a symmetric encoder–decoder, a bottleneck, and skip connections that shuttle high-resolution features from encoder to decoder [31, 32]. This design captures hierarchical spatial features while preserving fine detail, making it especially effective for pixel-level tasks (segmentation, denoising, reconstruction) compared with plain CNN classifiers. Accordingly, U-Nets are widely used in biomedicine for white-blood-cell and brain-tumor segmentation [33, 34]. In science, U-Nets have been utilized, for example, to segment 3D tomography of Polyamide-66 [35] and for analyzing rock-physics microstructures from CT/SEM to estimate porosity/connectivity [36]. In the context of QDs, U-Nets were implemented for the detection of unintentional QDs [12], in QD device virtualization system [10], and to classifying QD charge states by detecting transition edges in CSDs [37].

In this work, we use a compact encoder–decoder with two down- and two up-sampling stages. The encoder consists of  $3\times 3$  convolutions with ReLU activations and 0.3 dropout, followed by  $2\times 2$  max pooling. The decoder mirrors this structure using transposed convolutions and skip connections from the corresponding encoder layers. The network produces a feature map with five channels, which is then pooled via adaptive average pooling to generate a final output tensor of shape  $1\times 5$  for a single input sample.

#### 2.5 Vision transformers

Transformers, originally developed for natural-language processing [38, 39], have been successfully adapted to images with the vision transformers (ViT), which tokenize an image into patches and apply self-attention over the resulting sequence [40]. ViTs achieve competitive performance on image-recognition benchmarks and offer strong inductive flexibility relative to fixed local filters in CNNs [41]. In the physical sciences, variants of ViTs have been explored for end-to-end classification of quark- and gluon-initiated jets [42], for identifying particle-orbit types from Poincaré cross sections [43], and for detecting non-Abelian Majorana zero modes in disordered systems [44].

We use a compact ViT for  $30\times 30$  CSD patches. Each image is split into non-overlapping  $5\times 5$  patches, yielding a  $6\times 6$  grid (36 tokens), which are linearly embedded into a 128-dimensional space and augmented with a learnable class token and 2D positional embeddings. The encoder comprises six transformer layers, each with four attention heads, and a 512-dimensional feed-forward subnetwork. The class token is passed to an MLP head (256, then 128 units) that outputs predictions across 5 classes. This transformer baseline tests whether long-range, content-adaptive attention over CSD patches offers tangible gains over convolutional and MLP inductive biases at matched model size and training budget.

#### 2.6 Mixture density networks

Mixture density networks (MDNs) combine a feed-forward neural network with a parametric mixture model, predicting mixture weights, means, and variances to represent multi-modal conditional distributions [45, 46]. Although the canonical MDN is a regression model [47], recent variants adapt MDNs to classification by mapping mixture parameters through cumulative distribution functions (CDFs) and learning class logits—an approach we adopt via the MDN-C1 formulation [48]. MDNs have been used to identify clusters of multiple charged particles and estimate their corresponding hit positions [49]. In cosmology, they have been applied to determine photometric redshifts of extragalactic sources [50]. MDNs were also used to jointly infer layer numbers, depths, and the full probability distributions of S-wave velocities from wave dispersion curves [51]. While MDNs were not previously implemented in the QD context, they provide a principled approach to capturing label uncertainty arising from low-contrast transitions or overlapping features in CSD patches.

We implement an MDN-C1 classifier operating on flattened  $30\times 30$  CSD patches (900 inputs). A single hidden layer with 128  $\tanh$  units predicts the parameters of a three-component Gaussian mixture: weights, means, and positive standard deviations (enforced via a **softplus** activation). For each component, the Gaussian CDF is evaluated at every input dimension; the concatenated CDF features are passed to a final linear layer that outputs five-way class logits.

#### 2.7 ML models configuration

All models are trained with the AdamW optimizer [52]. Details about training hyperparameters for all models are presented in table 1. Since the labels are expressed as probability distributions, we chose the **KLDivLoss** as the loss function to account for the fractional labels. Each model is trained for up to 150 epochs with early stopping, with patience set to 10 epochs on the validation loss to



**Table 1.** Configuration for the AdamW optimizer hyperparameters used all models.  $\eta$  scheduler indicates whether the CosineAnnealingLR (cosine) or the constant learning rate was used.

| Hyperparameter       | CNN      | U-Net  | ViT    | MDN    |
|----------------------|----------|--------|--------|--------|
| Learning rate $\eta$ | 0.0005   | 0.0005 | 0.0001 | 0.0010 |
| Weight decay         | 0.0002   | 0.0001 | 0.0003 | 0.0001 |
| $\eta$ scheduler     | constant | cosine | cosine | cosine |

avoid overfitting. Finally, building on the deep ensembles approach, we implement an iterative 10-fold cross-validation to estimate models’ predictive uncertainty [53].

When discussing models’ performance, we report the *MSE score* defined as  $(1 - \text{MSE})$  to grant partial credit for calibrated probabilities. We consider two test datasets: the 9,900 samples from the original dataset; and a set of 756 manually labeled small experimental CSDs included in the QFlow 2.0 dataset.

### 2.8 *GitHub repository*

As part of this work, we release an open-source repository that provides a unified training and evaluation framework for the model families studied here (CNN, U-Net, ViT, and MDN). The toolkit ensures comparability across architectures via stratified  $k$ -fold cross-validation, programmatic control of data budgets (25/50/75/100 %), and seeded randomness for all sampling operations (fold assignment and subset selection) to guarantee reproducibility. All experiment settings are specified in human-readable YAML files, with per-model control over architecture toggles, optimizers, learning-rate schedulers, normalization (z-score or *min-max*), and early-stopping criteria. A single CLI command orchestrates data preparation (including image-size unification to  $30 \times 30$ ), training, and evaluation, and it records the exact software environment and Git commit for provenance.

The framework automatically stores outputs in a structured layout: best-epoch checkpoints (`.pth`); per-fold metrics (fractional label MSE score and accuracy); training/validation curves; confusion matrices and calibration plots; and machine-readable logs (`.json/.csv`) for post hoc analysis and aggregation. Together, these features enable transparent and reproducible benchmarking of classical and deep models on QFlow 2.0, facilitating fair comparisons in future autotuning studies.

## 3 Results

In this section, we present the results of our benchmarking study, organizing them around (i) computational cost, (ii) predictive performance, and (iii) trade-off between them. We begin by quantifying the training requirements of each architecture, including the number of trainable parameters, memory footprint, and wall-clock time on GPU and CPU. This allows us to compare how the structural complexity of the CNN, U-Net, ViT, and MDN translate into resource demands and convergence behavior across dataset budgets. We then evaluate state-recognition performance as a function of training set size, before combining these results with training and inference costs to determine accuracy-efficiency trade-offs.

Training was performed using both min-max and z-score normalization methods on HTCCondor resources [54], which provided shared disk space and GPU/CPU allocations. The model configuration and computational requirements summary are presented in table 2. Overall, we observe a loose correlation between the number of trainable parameters and total training time. The U-Net incurs the highest computational cost under both normalization schemes (with about 22 and 24 GPU hours and 27 and 31 CPU hours for z-score and min-max, respectively), consistent with the overhead of its spatially intensive layers and skip connections. The ViT also exhibits relatively high training times (about 12 and 22 GPU hours and 15 and 29 CPU hours for z-score

**Table 2.** Training configuration and computational requirements for all evaluated models. The table reports the number of trainable parameters, memory allocation, and training times on GPU and CPU under both min-max and z-score normalization schemes.

| Metric                          |           | CNN    | U-Net  | ViT    | MDN    |
|---------------------------------|-----------|--------|--------|--------|--------|
| No. of trainable parameters [M] |           | 0.06   | 1.86   | 1.27   | 0.83   |
| Space allocation [GB]           |           | 2.3(1) | 3.5(0) | 3.1(0) | 2.8(1) |
| GPU [h]                         | {min-max} | 18.0   | 23.8   | 21.7   | 12.4   |
| CPU [h]                         |           | 24.7   | 30.5   | 28.5   | 16.7   |
| GPU [h]                         | {z-score} | 16.2   | 21.6   | 12.2   | 5.9    |
| CPU [h]                         |           | 21.0   | 26.5   | 15.2   | 7.6    |

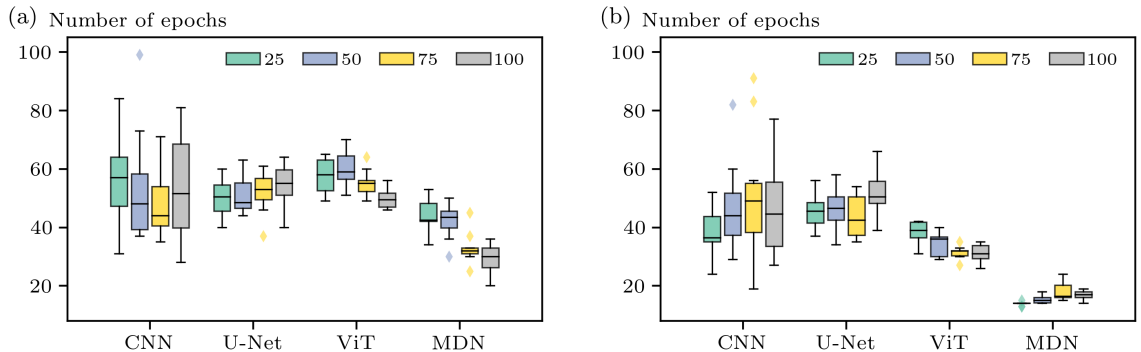


**Figure 3.** Box plots illustrating the distribution of the number of epochs for each class of models trained on data normalized using (a) min-max and (b) z-score. The colors correspond to the four data budgets: 25 % (green), 50 % (blue), 75 % (yellow), and 100 % (gray), respectively.

and min-max, respectively) and one of the largest memory footprints (about 3.1 GB), driven by attention matrices and high-dimensional embeddings. In contrast, the MDN is most efficient, benefiting from avoiding spatial tensor operations altogether and achieving the shortest GPU and CPU runtimes.

Memory usage mirrors these architectural differences: the U-Net requires the most memory (3.5 GB regardless of normalization), followed by the ViT. The CNN and MDN remain in the 2.3 to 2.8 GB range due to their comparatively small intermediate tensors. Across all architectures, the choice of normalization has only a modest effect on runtime and memory consumption, with min-max normalization tending to be slightly more resource-intensive than z-score normalization.

The impact of the normalization scheme on training dynamics is summarized in figure 3. For min-max normalization, we observe substantial variability in the number of epochs required for convergence, with CNNs being the least stable and slowest to converge, and MDNs being the most stable and fastest to converge, regardless of normalization and data budgets. This increased spread for CNNs suggests that the optimizer is failing to reach a consistent stopping point across folds. Interestingly, for the 75 % data budget, all min-max-normalized models exhibit noticeably reduced variability, indicating that the adverse effects of min-max scaling are partially mitigated at this intermediate data fraction.

In contrast, with the exception of CNN, z-score normalization yields considerably tighter epoch distributions across all models and dataset sizes, pointing to more stable and predictable training behavior. This trend is particularly evident in the MDN models, where the box plots show narrower interquartile ranges and fewer outliers, indicating more consistent convergence with fewer epochs. The z-score normalization appears to facilitate a more stable and predictable training process, contributing to more uniform performance across varying dataset sizes.

The performance of all models considered in this work is presented in figure 4, with the top panel depicting inference on simulated data and the bottom panel showing inference on experimental data. Unsurprisingly, the models perform better overall on simulated data, with the highest accuracy and lowest variability consistently observed under min-max normalization. This likely reflects the more controlled and homogeneous nature of the simulated distributions, where min-max scaling preserves informative relative differences between features and thereby facilitates training.

For the simulated data, model performance differs noticeably between normalization methods. Under min-max normalization, all models achieve MSE scores above 0.98, whereas under z-score normalization, the average MSE score drops to roughly 0.7 to 0.8 for CNN and U-Net and about 0.7 for ViT and MDN. The inset in figure 4(a) shows that for min-max normalization, accuracy generally improves with increasing data budget. For z-score normalization, the accuracy increases with data budget for CNN and U-Net, but remains fairly constant for ViT and MDN. The overall rankings, from highest to lowest performing models, are U-Net, ViT, CNN, and MDN under min-max normalization, and U-Net, CNN, and indistinguishably ViT and MDN under z-score normalization. However, even for the best-performing models, the variability across runs is substantially larger under z-score than under min-max normalization, where most runs converge around 0.99 MSE score.

For the experimental data, we again observe qualitative differences between the two normalization schemes, though not as dramatic as for the simulated data. Under min-max normalization, the best-performing model is CNN, followed by U-Net, with the latter having

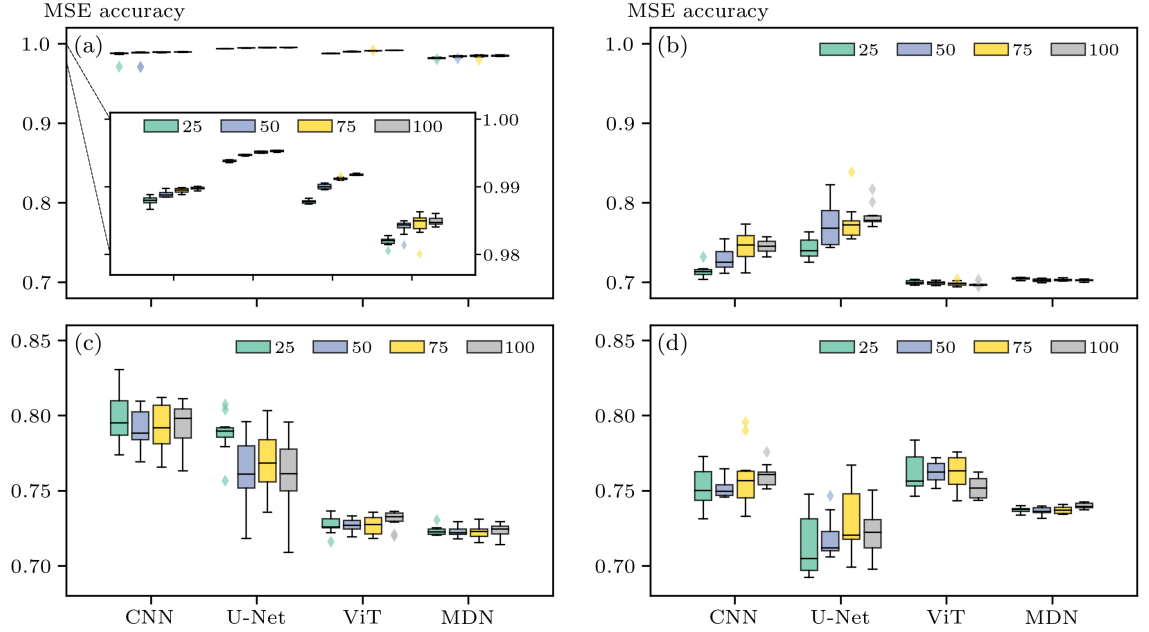


**Figure 4.** MSE score for (a-b) simulated and (c-d) experimental test datasets across all models. Models trained using min-max normalization are shown in panels (a) and (c), while panels (b) and (d) show models trained using z-score normalization. The colors correspond to the four data budgets: 25 % (green), 50 % (blue), 75 % (yellow), and 100 % (gray), respectively.

significantly higher fold-to-fold variance. The ViT and MDN achieve lower accuracy but display tighter MSE distributions. Under z-score normalization, the best-performing models are CNN and ViT, again with high variability in accuracy across epochs. In contrast, U-Net performs unexpectedly poorly and remains unstable. The MDN yields tightly clustered MSE distributions and relatively stable performance. Although experimental data yield lower MSE scores across all models, min-max normalization still confers a relative advantage in most cases, suggesting that it provides a robust default scaling strategy even in noisier, more heterogeneous regimes. The overall rankings, from highest to lowest performing models, are CNN, U-Net, ViT, and MDN under min-max normalization, and ViT, CNN, MDN, and U-Net under z-score normalization.

Taken together, our results highlight clear trade-offs between computational cost and predictive performance across architectures, which are further modulated by the choice of normalization and the nature of the data. U-Net sits at the “high-cost, high-accuracy” end of the spectrum when tested on simulated data for both normalization strategies: it consistently achieves the highest MSE score, but at the expense of the largest memory footprint and the longest GPU and CPU training times. Moreover, its performance decreases significantly on experimental data, especially for z-score normalization, rendering the training cost unjustified. CNNs occupy an intermediate regime with moderate computational demands and strong performance on both simulated and experimental data, across both normalization strategies. However, its training dynamics are less stable, with large fold-to-fold variability in the number of epochs and MSE score. By contrast, MDN defines the “lightweight” end of the spectrum, offering substantially lower training costs and more stable convergence, albeit with a modest loss in peak accuracy relative to CNNs and U-Nets.

#### 4 Conclusion and outlook

In this paper, we present a benchmarking study of modern deep ML models for multi-class state recognition in DQD CSDs. By systematically varying the data budget, normalization scheme, and model architecture on the QFlow 2.0 dataset [13], we provide a controlled comparison of predictive performance and computational cost directly relevant to the design of automated QD tuning protocols.

On synthetic data, the U-Net achieved the highest MSE scores, featuring its ability to capture hierarchical spatial features, which are crucial for identifying charge transition patterns. This performance, however, comes at a high computational cost, as U-Nets require the longest training times and the highest memory allocations among all models. Moreover, their performance degrades noticeably on experimental data, especially under z-score normalization, which limits the practical value of the additional complexity. At the opposite end of the spectrum, the computationally



cheaper MDN models offer very stable training dynamics and the shortest GPU and CPU runtimes, but yield significantly lower MSE scores on both synthetic and experimental data. Between these extremes, the CNN and ViT provide an attractive compromise, with CNN in particular delivering strong performance on experimental data despite having an order of magnitude fewer parameters than U-Net and ViT.

When tested on experimental data, convolution-based networks (CNN and U-Net) consistently seem to perform significantly better under min-max normalization (by about 4 – 5 %) at the cost of greater variation between folds and reduced training stability (more training needed on average), and hence more compute, while the ViT and MDN improved (by about 3 %) under z-score normalization conditions with fewer epochs on average. Thus, in real-world applications, the success of these models might depend strongly on the data preprocessing approach. In the context of QD data, min-max normalization yields the best overall performance, suggesting that it provides a more robust preprocessing approach for automated QD tuning systems, particularly in deployments where noise floors vary.

Overall, our benchmarking study indicates that no single architecture dominates across all regimes. Instead, practitioners should select models along the accuracy–efficiency frontier that best match the available compute and the target operating conditions. On synthetic CSDs, min–max normalization tends to amplify the performance gap in favor of more expressive models: U-Net and ViT yield the highest accuracies with relatively low variance across data budgets. However, the lack of generalizability to out-of-distribution data significantly limits the utility of such models, as they rely heavily on labeled experimental datasets for training, which are not readily available at present. Given that at present only simulated data are readily available for training, our results suggest that middle-ground CNN models combined with min-max normalization and careful regularization offer the best balance between accuracy and cost and are the best solution for real-time calibration of state in QD devices.

Looking ahead, several extensions of this work are natural. First, expanding the benchmark to include larger QD-array data, additional material platforms, and more diverse simulated data could help quantify the robustness of these conclusions beyond the DQD setting. Second, domain-adaptation and transfer-learning strategies—such as fine-tuning on small experimental sets or incorporating physics-informed priors—could improve the generalization of high-capacity models trained predominantly on simulations. Finally, incorporating uncertainty quantification and explainability tools could support safer ML use in QD tuning by enabling end users to interrogate model confidence and failure modes. Together, these directions can help translate benchmarking results into practical, trustworthy components for automated control of large-scale QD devices.

### Acknowledgments

The views and conclusions contained in this paper are those of the authors and should not be interpreted as representing the official policies, either expressed or implied, of the U.S. Government. The U.S. Government is authorized to reproduce and distribute reprints for Government purposes, notwithstanding any copyright noted herein. Any mention of commercial products is for information only; it does not imply recommendation or endorsement by NIST.

### References

- [1] G. Burkard, T. D. Ladd, A. Pan, J. M. Nichol, and J. R. Petta. Semiconductor spin qubits. *Rev. Mod. Phys.*, 95(2):025003, 2023.
- [2] L. M. K. Vandersypen and M. A. Eriksson. Quantum computing with semiconductor spins. *Phys. Today*, 72(8):38–45, 2019.
- [3] R. Hanson, L. P. Kouwenhoven, J. R. Petta, S. Tarucha, and L. M. K. Vandersypen. Spins in few-electron quantum dots. *Rev. Mod. Phys.*, 79(4):1217–1265, 2007.
- [4] D. M. Zajac, T. M. Hazard, X. Mi, E. Nielsen, and J. R. Petta. Scalable gate architecture for a one-dimensional array of semiconductor spin qubits. *Phys. Rev. Appl.*, 6(5):054013, 2016.
- [5] W. G. van der Wiel, S. De Franceschi, J. M. Elzerman, T. Fujisawa, S. Tarucha, and L. P. Kouwenhoven. Electron transport through double quantum dots. *Rev. Mod. Phys.*, 75(1):1–22, 2002.
- [6] J. P. Zwolak and J. M. Taylor. *Colloquium: Advances in automation of quantum dot devices control*. *Rev. Mod. Phys.*, 95(1):011006, 2023.

- [7] J. P. Zwolak, T. McJunkin, S. S. Kalantre, J.P. Dodson, E. R. MacQuarrie, D.E. Savage, M.G. Lagally, S.N. Coppersmith, M. A. Eriksson, and J. M. Taylor. Autotuning of double-dot devices in situ with machine learning. *Phys. Rev. Appl.*, 13(3):034075, 2020.
- [8] R. Durrer, B. Kratochwil, J.V. Koski, A.J. Landig, C. Reichl, W. Wegscheider, T. Ihn, and E. Greplova. Automated tuning of double quantum dots into specific charge states using neural networks. *Phys. Rev. Appl.*, 13(5):054019, 2020.
- [9] J. Ziegler, F. Luthi, M. Ramsey, F. Borjans, G. Zheng, and J. P. Zwolak. Tuning arrays with rays: Physics-informed tuning of quantum dot charge states. *Phys. Rev. Appl.*, 20(3):034067, 2023.
- [10] A. S. Rao, D. Buterakos, B. van Straaten, V. John, C. X. Yu, S. D. Oosterhout, L. Stehouwer, G. Scappucci, M. Veldhorst, F. Borsoi, and J. P. Zwolak. Modular Autonomous Virtualization System for Two-Dimensional Semiconductor Quantum Dot Array. *Phys. Rev. X*, 15(2):021034, 2025.
- [11] G. A. Oakes, J. Duan, J. J. L. Morton, A. Lee, C. G. Smith, and M. F. G. Zalba. Automatic virtual voltage extraction of a  $2 \times 2$  array of quantum dots with machine learning. *arXiv:2012.03685*, 2024.
- [12] J. Ziegler, F. Luthi, M. Ramsey, F. Borjans, G. Zheng, and J. P. Zwolak. Automated extraction of capacitive coupling for quantum dot systems. *Phys. Rev. Appl.*, 19(5):054077, 2023.
- [13] National Institute of Standards and Technology. Qflow 2.0: Quantum dot data for machine learning. Database: data.nist.gov, <https://doi.org/10.18434/T4/1423788>, 2022.
- [14] V. Gualtieri, C. Renshaw-Whitman, V. Hernandez, and E. Greplova. Qdsim: A user-friendly toolbox for simulating large-scale quantum dot devices. *SciPost Phys. Codebases*, page 46, 2025.
- [15] B. van Straaten, J. Hickie, L. Schorling, J. Schuff, F. Fedele, and N. Ares. Qarray: A gpu-accelerated constant capacitance model simulator for large quantum dot arrays. *SciPost Phys. Codebases*, page 35, 2024.
- [16] J. A. Krzywda, W. Liu, E. van Nieuwenburg, and O. Krause. QDarts: A quantum dot array transition simulator for finding charge transitions in the presence of finite tunnel couplings, non-constant charging energies and sensor dots. *SciPost Phys. Codebases*, page 43, 2025.
- [17] D. L. Buterakos, S. S. Kalantre, J. Ziegler, J. M. Taylor, and J. P. Zwolak. Qdflow: A python package for physics simulations of quantum dot devices. *arXiv:2509.13298*, 2025.
- [18] TBD. ML-mini suite. GitHub, 2025.
- [19] Christoph Kloeffer and Daniel Loss. Prospects for spin-based quantum computing in quantum dots. *Annu. Rev. Condens. Matter Phys.*, 4:51–81, 2013.
- [20] C. B. Simmons, M. Thalakulam, N. Shaji, L. J. Klein, H. Qin, R. H. Blick, D. E. Savage, M. G. Lagally, S. N. Coppersmith, and M. A. Eriksson. Single-electron quantum dot in Si/SiGe with integrated charge sensing. *Appl. Phys. Lett.*, 91(21):213103, 2007.
- [21] J. P. Zwolak, S. S. Kalantre, X. Wu, S. Ragole, and J. M. Taylor. QFlow lite dataset: A machine-learning approach to the charge states in quantum dot experiments. *PLoS ONE*, 13(10):e0205844, 2018.
- [22] S. S. Kalantre, J. P. Zwolak, S. Ragole, X. Wu, N. M. Zimmerman, M. D. Stewart, and J. M. Taylor. Machine learning techniques for state recognition and auto-tuning in quantum dots. *npj Quantum Inf.*, 5(1):6, 2019.
- [23] Alex Krizhevsky, Ilya Sutskever, and Geoffrey E. Hinton. Imagenet classification with deep convolutional neural networks. In *Advances in Neural Information Processing Systems 25 (NeurIPS)*, pages 1097–1105, 2012.

- [24] F. Oviedo, Z. Ren, S. Sun, C. Settens, Z. Liu, N. T. P. Hartono, S. Ramasamy, B. L. DeCost, S. I. P. Tian, G. Romano, A. G. Kusne, and T. Buonassisi. Fast and interpretable classification of small x-ray diffraction datasets using data augmentation and deep neural networks. *npj Comput. Mater.*, 5:60, 2019.
- [25] A. Ziletti, D. Kumar, M. Scheffler, and L. M. Ghiringhelli. Insightful classification of crystal structures using deep learning. *Nat. Commun.*, 9:2775, 2018.
- [26] S. Dieleman, K. W. Willett, and J. Dambre. Rotation-invariant convolutional neural networks for galaxy morphology prediction. *Mon. Not. R. Astron. Soc.*, 450(2):1441–1459, 2015.
- [27] M. Ziatdinov, O. Dyck, A. Maksov, X. Li, X. Sang, K. Xiao, R. R. Unocic, R. Vasudevan, S. Jesse, and S. V. Kalinin. Deep learning of atomically resolved scanning transmission electron microscopy images: Chemical identification and tracking local transformations. *ACS Nano*, 11(12):12742–12752, 2017.
- [28] V. Yon, B. Galaup, C. Rohrbacher, J. Rivard, A. Morel, D. Leclerc, C. Godfrin, R. Li, S. Kubicek, K. De Greve, E. Dupont-Ferrier, Y. Beilliard, R. G. Melko, and D. Drouin. Experimental online quantum dots charge autotuning using neural network. *arXiv:2409.20320*, 2024.
- [29] J. Ziegler, T. McJunkin, E. S. Joseph, S. S. Kalantre, B. Harpt, D. E. Savage, M. G. Lagally, M. A. Eriksson, J. M. Taylor, and J. P. Zwolak. Toward robust autotuning of noisy quantum dot devices. *Phys. Rev. Appl.*, 17(2):024069, 2022.
- [30] A. B. Mei, I. Milosavljevic, A. L. Simpson, V. A. Smetanka, C. P. Feeney, S. M. Seguin, S. D. Ha, W. Ha, and M. D. Reed. Optimization of quantum-dot qubit fabrication via machine learning. *Appl. Phys. Lett.*, 118(20):204001, 2021.
- [31] O. Ronneberger, P. Fischer, and T. Brox. U-Net: Convolutional Networks for Biomedical Image Segmentation. In *Medical Image Computing and Computer-Assisted Intervention – MICCAI 2015*, pages 234–241. Springer International Publishing, 2015. On behalf of the ATLAS Collaboration.
- [32] X.-C. Tai, H. Liu, R. H. Chan, and L. Li. A mathematical explanation of UNet. *Math. Found. Comput.*, 8(5):874–889, 2025.
- [33] A. H. Alharbi, C. V. Aravinda, M. Lin, P. S. Venugopala, P. Reddicherla, and M. A. Shah. Segmentation and classification of white blood cells using the unet. *Contrast Media Mol. Imaging*, 2022:5913905, 2022.
- [34] P. Agrawal, N. Katal, and N. Hooda. Segmentation and classification of brain tumor using 3d-unet deep neural networks. *Int. J. Cogn. Comput. Eng.*, 3:199–210, 2022.
- [35] J. P. C. Bertoldo, E. Decenci re, D. Ryckelynck, and H. Proudhon. A modular u-net for automated segmentation of x-ray tomography images in composite materials. *Front. Mater.*, 8:761229, 2021.
- [36] Z. Ma, X. He, H. Kwak, J. Gao, S. Sun, and B. Yan. Enhancing rock image segmentation in digital rock physics: A fusion of generative ai and state-of-the-art neural networks. *arXiv:2311.06079*, 2023.
- [37] F. Hader, F. Fuchs, S. Fleitmann, K. Havemann, B. Scherer, J. Vogelbruch, L. Geck, and S. van Waasen. Automated charge transition detection in quantum dot charge stability diagrams. *IEEE Trans. Quantum Eng.*, 6:1–14, 2025.
- [38] A. Vaswani, N. Shazeer, N. Parmar, J. Uszkoreit, L. Jones, A. N. Gomez,  . Kaiser, and I. Polosukhin. Attention is all you need. In *Advances in Neural Information Processing Systems*, volume 30, 2017.
- [39] T. Brown, B. Mann, N. Ryder, M. Subbiah, J. D. Kaplan, P. Dhariwal, A. Neelakantan, P. Shyam, G. Sastry, A. Askell, and *et al*. Language models are few-shot learners. In *Advances in Neural Information Processing Systems*, volume 33, pages 1877–1901, 2020.
- [40] A. Dosovitskiy, L. Beyer, A. Kolesnikov, D. Weissenborn, X. Zhai, T. Unterthiner, M. Dehghani, M. Minderer, G. Heigold, S. Gelly, J. Uszkoreit, and N. Houlsby. An image is worth 16 16 words: Transformers for image recognition at scale. *arXiv:2010.11929*, 2021.

- [41] K. Han, Y. Wang, H. Chen, X. Chen, J. Guo, Z. Liu, Y. Tang, A. Xiao, C. Xu, Y. Xu, Z. Yang, Y. Zhang, and D. Tao. A survey on vision transformer. *IEEE Trans. Pattern Anal. Mach. Intell.*, 45(1):87–110, Jan 2023.
- [42] A. Jahin, S. Soudeep, A. R. Aditta, M. F. Mridha, N. Fahad, and J. Hossein. Vision transformers for end-to-end quark-gluon jet classification from calorimeter images. *arXiv:2506.14934*, 2025.
- [43] Y. Sun. Poincare cross section classification based on vision transformer. In *2023 International Conference on Mechatronics, IoT and Industrial Informatics (ICMIII)*, pages 174–178, Melbourne, Australia, 2023.
- [44] J. R. Taylor and S. Das Sarma. Vision transformer based deep learning of topological indicators in majorana nanowires. *Phys. Rev. B*, 111(10):104208, 2025.
- [45] C. M. Bishop. Mixture density networks. Working paper, Aston University, 1994.
- [46] O. Makansi, E. Ilg, Ö. Çiçek, and T. Brox. Overcoming limitations of mixture density networks: A sampling and fitting framework for multimodal future prediction. In *2019 IEEE/CVF Conference on Computer Vision and Pattern Recognition (CVPR)*, pages 7137–7146. IEEE, 2019.
- [47] A. Brando. *Mixture Density Networks (MDN) for distribution and uncertainty estimation*. PhD thesis, Universitat de Barcelona, Barcelona, Spain, 2017.
- [48] N. Gugulothu, S. P. Bhat, and T. Bodas. Mixture density networks for classification with an application to product bundling. *arXiv:2402.05428*, 2024.
- [49] Elham E. Khoda. ATLAS pixel cluster splitting using mixture density networks. In *7th Annual Conference on Large Hadron Collider Physics (LHCP2019)*, page 009. PoS Proc. Sci, 2017. On behalf of the ATLAS Collaboration.
- [50] Z. Ansari, A. Agnello, and C. Gall. Mixture models for photometric redshifts. *Astron. Astrophys.*, 650:A90, 2021.
- [51] S. Keil and J Wassermann. Surface wave dispersion curve inversion using mixture density networks. *Geophys. J. Int.*, 235:401–415, 2023.
- [52] I. Loshchilov and F. Hutter. Decoupled weight decay regularization. *arXiv:1711.05101*, 2017.
- [53] B. Lakshminarayanan, A. Pritzel, and C. Blundell. Simple and scalable predictive uncertainty estimation using deep ensembles. In *Adv. Neural Inf. Process. Syst.*, volume 30, 2017.
- [54] B. Bockelman, M. Livny, B. Lin, and F. Prelz. Principles, technologies, and time: The translational journey of the htcondor-ce. *J. Comput. Sci.*, 52:101213, 2020.